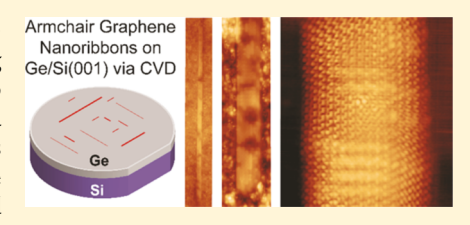


# Synthesis of Armchair Graphene Nanoribbons on Germanium-on-Silicon

Vivek Saraswat, † Yuji Yamamoto, † Hyun Jung Kim, Robert M. Jacobberger, † Katherine R. Jinkins, † Austin J. Way, 10 Nathan P. Guisinger, 10 and Michael S. Arnold\*, 1

Supporting Information

ABSTRACT: The synthesis of graphene nanoribbons on complementary metal oxide-semiconductor-compatible substrates is a significant challenge hindering their integration into commercial semiconductor electronics. Here, the bottom-up synthesis of armchair graphene nanoribbons on epilayers of Ge on Si(001) via chemical vapor deposition is demonstrated. The synthesis leverages the previous discovery that graphene crystal growth can be driven with an extreme shape anisotropy on Ge(001) surfaces to directly form nanoribbons. However, compared to nanoribbon synthesis on Ge(001), synthesis on Ge/Si(001) is complicated by



the possibility of Si diffusion to the Ge surface and the presence of threading dislocations. Herein, we demonstrate that similar to Ge(001), armchair nanoribbons with faceted edges and sub-10 nm widths can indeed be grown on Ge/Si(001). The nanoribbon synthesis proceeds faster than the diffusion of Si to the Ge surface if a sufficiently thick Ge epilayer is used (e.g., 3  $\mu$ m), thereby avoiding competing reactions that form SiC. Moreover, threading dislocations in the Ge epilayer are not observed to affect the nucleation or anisotropic growth kinetics of the nanoribbons. These results demonstrate that previous successes in graphene nanoribbon synthesis on Ge(001) can be extended to Si(001) by using epilayers of Ge, motivating the future exploration of this promising platform for hybrid semiconducting graphene/Si electronics.

#### ■ INTRODUCTION

Graphene nanoribbons are narrow stripes of graphene that can be semiconducting and exhibit high carrier mobility, 1,2 high current carrying capacity,<sup>3</sup> and tunable band gap.<sup>4,5</sup> Because of their unique characteristics, graphene nanoribbons are being explored as promising candidates for next-generation nanoelectronic devices<sup>6</sup> for semiconductor logic,<sup>7,8</sup> high-frequency communications,<sup>9,10</sup> and sensing applications.<sup>11,12</sup> Recently, the production of graphene nanoribbons has been demonstrated by several methods, including top-down lithographic patterning of monolayer graphene, <sup>13</sup> unzipping of graphite <sup>14</sup> and carbon nanotubes, <sup>15</sup> solution- <sup>16,17</sup> and surface- <sup>18–20</sup> assisted synthesis using organic precursors, templated growth on SiC,<sup>21</sup> and chemical vapor deposition (CVD) growth on Ge.<sup>22</sup> Of these, the bottom-up synthesis on Ge(001) using CVD is studied here and is particularly attractive because of its wafer-scale scalability, width, and length tunability and because it offers a viable route for direct synthesis on a semiconducting platform.<sup>22-23</sup>

During graphene synthesis on Ge(001), a carbon precursor such as CH<sub>4</sub> or C<sub>2</sub>H<sub>4</sub> is introduced to the Ge surface at elevated temperatures (~900 °C) in the presence of H<sub>2</sub>, enabling the catalytic decomposition of the precursor. 26,27 The reactive intermediate species that result from decomposition (such as C, CH, CH<sub>2</sub>, and CH<sub>3</sub>) diffuse on the surface and

form graphene nuclei.<sup>28</sup> For large supersaturation of these intermediate species, these nuclei quickly evolve into large graphene crystals with relatively low aspect ratio, and eventually, these crystals merge to form a continuous layer of graphene. 29-33 In contrast, when the supersaturation and growth rate are low on Ge(001), these nuclei evolve anisotropically into highly elongated crystals, enabling the direct synthesis of graphene nanoribbons. 22,25 These nanoribbons have widths as narrow as 1.7 nm that are uniform along their lengths, exhibit smooth armchair edges, 25 which are critical for both high carrier mobility and a technologically relevant band gap, and are self-orienting along Ge(110) directions.<sup>25</sup> Furthermore, nanoribbons synthesized by CVD exhibit promising charge transport characteristics in field-effect transistors, which are a major advantage of this approach.<sup>34</sup> Although the spontaneous nucleation of nanoribbons on Ge(001) yields nanoribbons in random locations that have polydisperse widths and multiple orientations, arrays of more monodisperse and unidirectionally aligned graphene nanoribbons with rational placement can be realized by initiating synthesis from lithographically patterned graphene seeds.

Received: May 9, 2019 Revised: June 12, 2019 Published: July 9, 2019



Department of Materials Science & Engineering, University of Wisconsin—Madison, Madison, Wisconsin 53706, United States \*IHP—Libniz-Insitut für Innovative Mikroelektronik, Im Technologiepark 25, 15236 Frankfurt (Oder), Germany

<sup>&</sup>lt;sup>§</sup>National Institute of Aerospace, 100 Exploration Way, Hampton, Virginia 23666, United States

Center for Nanoscale Materials, Argonne National Laboratory, Argonne, Illinois 60439, United States

The Journal of Physical Chemistry C

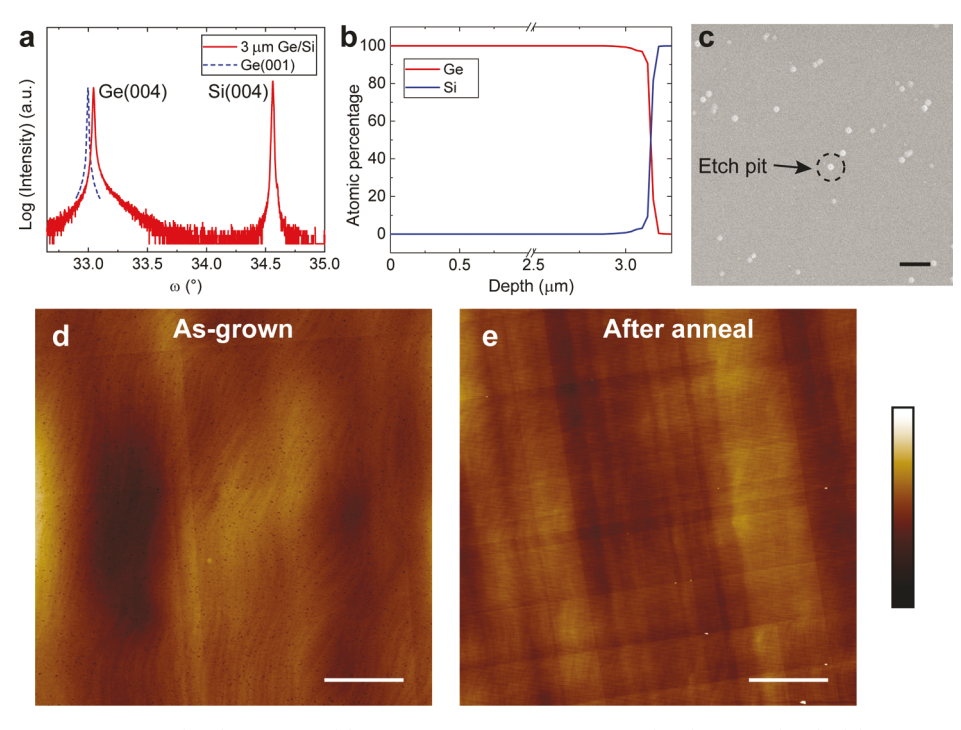


Figure 1. Characterization of the Ge/Si(001) substrate. (a)  $\omega$ -2 $\theta$  scans of as-grown Ge/Si(001) and Ge(001). (b) XPS depth profile of Ge(001)/Si(001) showing the composition of Ge and Si. (c) SEM micrograph of the Ge/Si(001) surface after a 3 min SECCO etch to reveal etch pits at threading dislocations. Scale bar is 5  $\mu$ m. AFM scans of the (d) as-grown Ge/Si(001) surface and (e) Ge/Si(001) after 30 min annealing at 910 °C. Scale bars in (d,e) are 2  $\mu$ m. Height scale bar is 10 nm.

Alignment can also be driven by conducting synthesis on vicinal Ge(001).<sup>23</sup> These seeding and alignment approaches could enable front-end-of-line integration of graphene nanoribbons in integrated circuits (ICs), with future improvements in the uniformity of seed size. Recent studies have shown that nanoribbon edge—substrate interactions are responsible for the nanoribbon anisotropic growth kinetics.<sup>23,24</sup> Reconstruction<sup>35</sup> and nanofaceting<sup>36,37</sup> of the substrate may also affect nanoribbon shape evolution.

Despite these promising advances, a critical limitation of the anisotropic synthesis of armchair graphene nanoribbons via CVD is that so far it has only been achieved on Ge(001) substrates. In contrast, Si, not Ge, historically has been the platform of choice for ICs. However, the CVD of graphene directly on Si is challenged by the stable formation of SiC at temperatures >800 °C. This challenge is demonstrated in Figure S1, in which the CVD of CH<sub>4</sub> on SiGe alloys containing only 15% Si yields SiC.

One possible solution to this problem is to transfer graphene nanoribbons grown on Ge(001) onto Si via a polymer-assisted wet-transfer<sup>33</sup> or a metal-assisted dry-transfer process.<sup>34</sup> However, such approaches are less desirable than direct growth because even if the yield of the transfer is 100%, these approaches can result in mechanical damage,<sup>41</sup> doping,<sup>42</sup> polymer residue,<sup>43,44</sup> and metallic contamination,<sup>45</sup> while degrading carrier mobility<sup>41</sup> and leading to irreproducible device characteristics.<sup>45</sup>

Here, a transfer-free approach for growing graphene nanoribbons on Si wafers is explored via the deposition and use of complementary metal—oxide—semiconductor (CMOS)-compatible epilayers of Ge. Prior work has shown that sacrificial catalytic layers such as Ni, Cu, Au, and Ag can be deposited onto  $\mathrm{SiO_2/Si}$  substrates,  $^{46-50}$  thereby enabling the synthesis or templated synthesis of graphene on these

substrates. However, these layers do not promote the anisotropic growth phenomena that are needed during CVD to drive the synthesis of armchair graphene nanoribbons. The patterning of these layers has also been used in attempts to template nanoribbons; however, such approaches have not succeeded in creating sub-10 nm nanoribbons with smooth armchair edges. \$2,53

Recently, continuous sheets of monolayer graphene have been synthesized on 200 mm diameter wafers of Si by CVD<sup>29,32</sup> and molecular beam epitaxy<sup>54</sup> via the use of epilayers of Ge. However, the synthesis of nanoribbons on this platform has not yet been demonstrated or studied. Of concern are (1) the effects of Si diffusion to the Ge surface, which are expected to be more pronounced at the slower growth rates and longer growth times that are needed to induce the anisotropic synthesis of nanoribbons and (2) the effects of dislocations in the Ge epilayer, which are always present in Ge epilayers deposited on Si because of lattice mismatch, on the nucleation or anisotropic growth kinetics of the nanoribbons. A comprehensive understanding of the influence of these factors, which has been missing from previous reports in the literature, is critical to realizing the full potential of graphene nanoribbons in electronics.

Here, we study the bottom-up synthesis of graphene nanoribbons on Ge/Si(001) via CVD. We show that by using a Ge epilayer that is 3  $\mu$ m in thickness and limiting the duration of nanoribbon synthesis (at 910 °C) to less than 9 h, significant Si diffusion to the surface can be avoided, resulting in graphene nanoribbon growth evolution and kinetics on Ge/Si(001) that are indistinguishable from those on Ge(001). Scanning tunneling microscopy (STM) shows that these nanoribbons have faceted armchair edges with low edge roughness and are semiconducting. <sup>22,25</sup> Moreover, threading dislocations in the Ge epilayers do not detrimentally affect the

The Journal of Physical Chemistry C

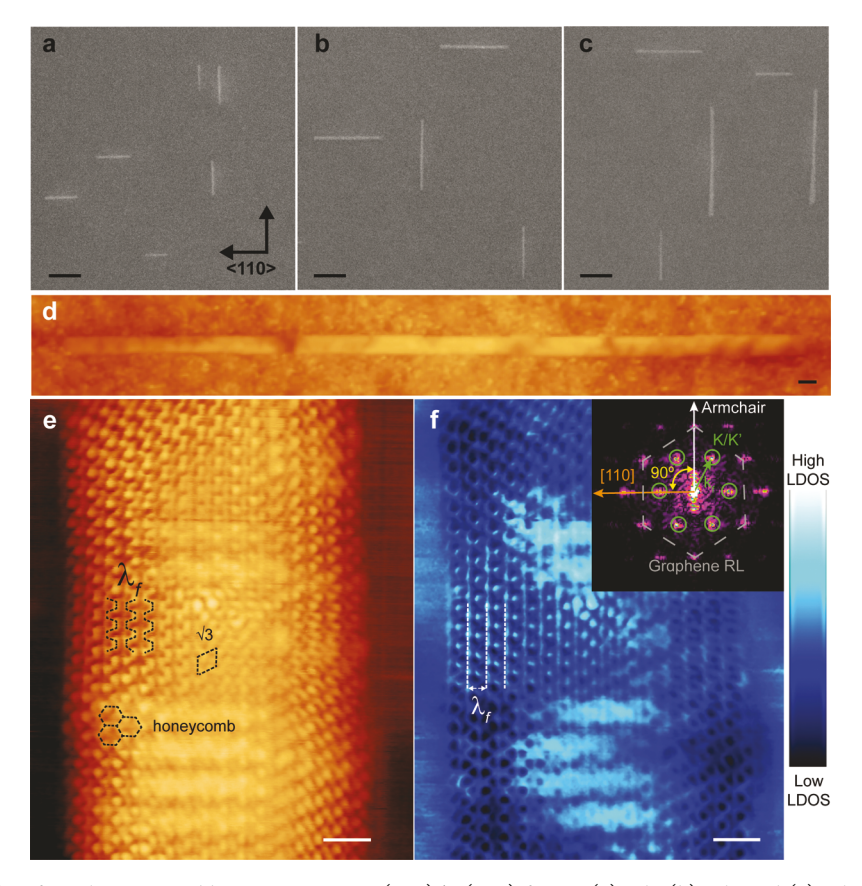


Figure 2. SEM micrographs of graphene nanoribbons grown on Ge(001)/Si(001) for t = (a) 3 h, (b) 6 h, and (c) 9 h. Growth conducted at 910 °C with  $x_{CH_4} = 6.6 \times 10^{-3}$  at ambient pressure. (d) STM image of a nanoribbon with w = 5 nm (applied bias = +2 V, tunneling current = 0.1 nA). (e) Atomically resolved STM topography of a nanoribbon grown using t = 3 h as in (a) (applied bias = +0.2 V, tunneling current = 1 nA). Intervalley scattering periodicity,  $\sqrt{3}$ , and honeycomb superperiodic interference patterns are highlighted. (f) Differential current image of the nanoribbon shown in (e) (V = 0.2 V) and its corresponding FFT image shown in the inset. Scale bars are 200 nm in (a-c) and 5, 1, and 1 nm in (d-f), respectively.

nucleation or anisotropic growth kinetics of the nanoribbons. These results suggest that previous work on graphene nanoribbon synthesis on  $\text{Ge}(001)^{22-25,34}$  can be translated to Ge/Si(001) and provide strong motivation for further research into the potential of Ge/Si(001) as a platform for integrated semiconducting graphene/Si devices.

## ■ RESULTS AND DISCUSSION

Characterization of Ge/Si(001) Substrates. Figure 1 characterizes the Ge/Si(001) substrates prior to nanoribbon synthesis. These substrates are fabricated by depositing epi-Ge on Si(001) using CVD, as described previously.<sup>55</sup> Figure 1a compares X-ray diffraction (XRD)  $\omega$ -2 $\theta$  scans of assynthesized Ge/Si(001) and Ge(001) substrates around the Ge(004) and Si(004) peaks. The high crystallinity of the Ge epilayer in Ge/Si(001) is evidenced by the presence of a sharp Ge(004) peak with a full width at half-maximum of 0.008°. In Ge/Si(001), the Ge(004) peak is shifted to a larger  $2\theta$  by 0.047°, indicating 0.7% tensile strain in the Ge epilayer that arises from differences in thermal expansion coefficients between Si and Ge.<sup>57</sup> The shoulder on the high angle side of the Ge(004) peak arises because of slight Si diffusion into Ge during the cyclic annealing step that is part of the Ge epitaxy, leading to the formation of interfacial SiGe. 56 Figure 1b shows an X-ray photoelectron spectroscopy (XPS) depth profile of the as-synthesized Ge/Si(001) substrate, which confirms that even though there is minor Si diffusion into Ge, there is a

relatively sharp interface between Ge and Si of 100 nm and that the thickness of the Ge epilayer is 3  $\mu$ m.

Figure 1c shows a scanning electron microscopy (SEM) image of the epilayer surface following a 3 min exposure to a SECCO etching solution (two parts HF + 1 part  $\rm H_2O$  + 0.15 M  $\rm K_2Cr_2O_7$ ). SE Etching in SECCO solution is commonly used to quantify threading dislocation density (TDD) in Si, Ge, and SiGe substrates, Secure 19 in which the density of etch pits generated by exposure to the SECCO solution quantifies the TDD. From the density of etch pits, we estimate the TDD to be 8.9 ×  $\rm 10^6~cm^{-2}$ , which is in agreement with previous work for TDD in Ge/Si(001) with similar Ge thicknesses grown via CVD. S5,61

Immediately before the nanoribbon synthesis, the substrates are annealed at 910 °C under a flow of 200 sccm of Ar and 100 sccm of  $\rm H_2$  at ambient pressure to remove  $\rm GeO_x$  and other volatile impurities from the surface. Figure 1d,e shows 10  $\mu \rm m$  × 10  $\mu \rm m$  atomic force microscopy (AFM) scans of Ge/Si(001) before and after annealing for 30 min, respectively. The root-mean-square (rms) roughness of the substrates marginally decreases from 0.8 to 0.6 nm during the annealing, ensuring low surface roughness prior to nanoribbon growth. After annealing, the  $\langle 110 \rangle$  cross-hatch pattern on the surface becomes more prominent, which is a signature of 60° threading dislocations along (111) planes that glide at the surface at high temperature.

Nanoribbon Orientation and Structure. Next, graphene nanoribbons are evolved on the Ge/Si(001) substrates using

CH<sub>4</sub> CVD at ambient pressure. A control Ge(001) substrate is placed next to the Ge/Si(001) substrates for comparison. Prior to these growths, the substrates are annealed for 30 min at 910 °C under a flow of 200 sccm of Ar and 100 sccm of H<sub>2</sub>. Then, 2 sccm of CH<sub>4</sub> is introduced (CH<sub>4</sub> mole fraction,  $x_{\text{CH}_4} = 6.6 \times$  $10^{-3}$ ) for different times (t = 2-14 h). Figure 2a-c shows representative SEM micrographs of the resulting nanoribbons on Ge/Si(001) after t = 3, 6, and 9 h of synthesis. The nanoribbons nucleate randomly on the surface (nucleation density  $\approx 2 \ \mu \text{m}^{-2}$ ), have widths that are uniform along their lengths and aspect ratios >20, and grow progressively longer with time. Electron backscatter diffraction (EBSD) data (Figure S2; see the Supporting Information for details) indicate that the nanoribbons are oriented roughly along equivalent (110) directions with equal probability, as seen previously on Ge(001).<sup>22</sup>

To gain further insight into the atomic structure and orientation of the nanoribbons, ultrahigh vacuum STM is used. Figure 2d shows a large-scale STM image of a nanoribbon synthesized with t = 3 h, as in Figure 2a (bias V = +2 V, tunneling current I = 0.1 nA, T = 55 K). The ribbon has a width of 5 nm and a length of 200 nm, yielding an aspect ratio of 40. The edges of the nanoribbon appear faceted over the entire length. To further investigate the edge structure of the nanoribbons, atomically resolved STM images are acquired. Figure 2e shows a constant-current STM image of a representative nanoribbon on Ge/Si(001) (bias V = +0.2 V, tunneling current I = 1 nA, T = 55 K), while Figure 2f shows a differential current map (dI/dV at sample bias V = +0.2 V, setpoint I = 1 nA) of the same nanoribbon. A fast Fourier transform (FFT) reciprocal space pattern of the differential current image is shown in the inset.

The STM data show that the edges of the nanoribbon are relatively smooth; for example, over the 10 nm ribbon length seen in Figure 2e, the width of the ribbon and edge roughness deviate by at most  $1a_0$  (where  $a_0$  is the lattice constant of graphene = 2.4 Å). Some of this apparent deviation can be attributed to perturbation of the STM tip by adsorbates and GeO<sub>x</sub> species on the bare Ge near the ribbon edges that make it difficult to precisely image edge topography. K/K' Brillouin zone points are visible in the FFT reciprocal space pattern and show that the armchair crystallographic orientation of the nanoribbons is parallel to the ribbon long axis. The orientation of the K/K' Brillouin zone points further confirms that the nanoribbons are roughly aligned with the (110) directions of the Ge substrate. Under the nanoribbons, the Ge surface adopts a (2 × 1) dimer reconstruction (Figure S3e). The ability of the STM to resolve the Ge surface reconstruction, through the nanoribbon, proves that the nanoribbons are monolayered.63,64

Electron interference effects are observed in both the constant current and differential current images.  $\lambda_f$  intervalley quasi-particle interference is observed at the edges of Figure 2e with a period of ~3.7 Å ( $\lambda_f = 3a_o/2$ ).  $\sqrt{3}$  and honeycomb superperiodic interference patterns are also observed in Figure 2e, indicating constructive interference along C-C bonds arising from electron back-scattering at pristine armchair edges.  $^{25,65-67}$  The  $\lambda_{\rm f}$  interference pattern is even more apparent in Figure 2f, which quantifies the electronic density of states at the tunneling bias. The interference pattern extends across the entire width of the nanoribbon as a result of its high structural fidelity. A dI/dV versus V point spectrum of a 5.7 nm

wide nanoribbon is analyzed in Figure S4 and shows that there is a gap in the density of states of the ribbon of 0.6 eV comparable to quasi-particle calculations<sup>5</sup> that predict a band gap in the range of 0.3-0.8 eV for this width (depending on the discrete width family). Additional STM data are presented

Nanoribbon Growth Kinetics. Figure 3 characterizes the average ensemble nanoribbon length (l) and width (w) versus

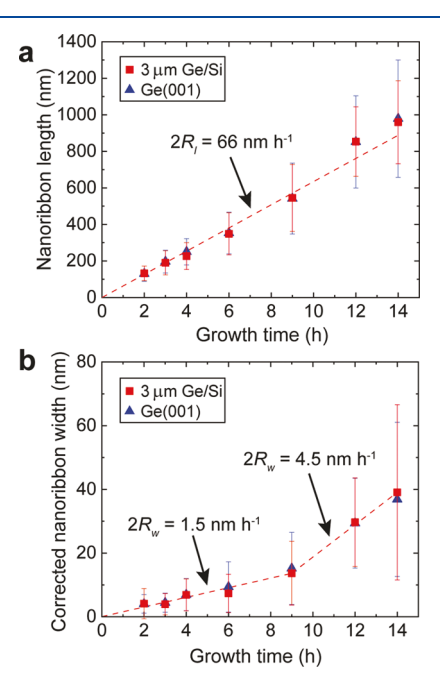


Figure 3. Growth kinetics and evolution of graphene nanoribbons. Plot of graphene nanoribbon (a) length and (b) width vs growth time on Ge/Si(001) and Ge(001). A correction factor of 5.64 nm is subtracted from each nanoribbon width because of blurring of the SEM beam (see the Supporting Information for details).

synthesis time (t) on Ge/Si(001) and Ge(001) at  $x_{CH_4} = 6.6$  $\times 10^{-3}$ ,  $x_{\rm H_2} = 0.33$ , and T = 910 °C. These growth parameters were selected upon optimization to yield nanoribbons with high aspect ratios (>30). It is known that in order to maximize the nanoribbon anisotropy the growth must be conducted close to the melting point of Ge and that the nanoribbon growth rate must be low.<sup>22</sup> Each datapoint in this figure characterizes the dimensions of 200 nanoribbons. The measured nanoribbon widths are subtractively corrected to account for broadening arising from the resolution limits of the SEM.<sup>68</sup> The resolution correction factor is determined by imaging a known reference sample of a single-walled carbon nanotube with a diameter of 1.5 nm<sup>69</sup> on Ge(001) (Figure S5), resulting in a 5.6 nm correction that is subtracted from the measured nanoribbon widths (details in the Supporting Information).

On both Ge/Si(001) and Ge(001), l increases linearly with t. The average nanoribbon growth rate in the length direction  $(R_l)$  is given as  $0.5 \times$  (slope of the linear fit of l vs t), where the factor of 0.5 arises because the nanoribbons grow outward along both directions along their length.  $R_l$  on Ge/Si(001) is 33 nm  $h^{-1}$  and is indistinguishable from that on Ge(001). The linearity of l versus t indicates that  $R_l$  remains constant with time. In contrast, w initially increases linearly with time, but w versus t becomes superlinear for t > 9 h. For example, the average growth rate in the width direction  $(R_w)$  is initially 0.8 nm h<sup>-1</sup> for t < 9 h, but  $R_w$  increases to 2.3 nm h<sup>-1</sup> for t > 14 h. The increase in  $R_w$  with time is comparable to behavior previously observed on Ge(001);<sup>22</sup> although the reason underpinning the superlinear behavior at longer times is not yet clear.

A noteworthy observation from these data is the substantial ribbon-to-ribbon variation in both the l versus t and w versus t plots at longer t, quantified by the error bars in Figure 3. This variation is primarily attributed to the continuous nucleation of nanoribbons throughout the growth duration (as opposed to variations in  $R_l$  or  $R_w$ ). Por instance, for a growth time of 12 h, some of the nanoribbons could have nucleated at t=2, 4, 6 h, etc., thereby yielding an effectively shorter growth time for these nanoribbons. Such polydispersity in l and w can be greatly diminished by using graphene seeds to initiate nanoribbon growth in a controlled fashion and by suppressing secondary nucleation, as demonstrated recently by Way et al.  $^{24,70}$ 

Next, the effect of CH<sub>4</sub> concentration  $(x_{CH_4})$  on  $R_l$  and  $R_w$  is investigated, as shown in Figure 4. The nanoribbons for these studies are grown at 910 °C at flow rates of Ar and H<sub>2</sub> of 200 and 100 sccm, respectively. The flow rate of CH<sub>4</sub> is varied from

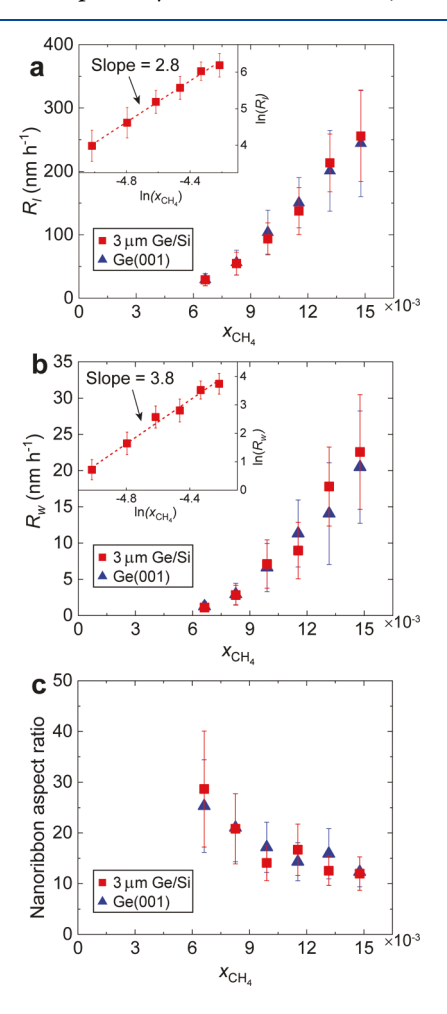


**Figure 4.** Effect of carbon precursor composition on nanoribbon growth. Plot of (a) length growth rate  $(R_l)$ , (b) width growth rate  $(R_w)$ , and (c) nanoribbon aspect ratio vs  $\alpha_{\rm CH_4}$  on Ge/Si(001) and Ge(001). The insets of (a,b) show the same data plotted on the loglog scale along with the best fit to extract empirical rate laws.

2 sccm ( $x_{\text{CH}_4} = 6.6 \times 10^{-3}$ ) to 4.5 sccm ( $x_{\text{CH}_4} = 1.47 \times 10^{-2}$ ). The duration of the synthesis is varied from 0.75 to 6 h, depending on  $x_{\text{CH},l}$ , so that nanoribbons of  $l \ge 300$  nm and  $w \ge 10^{-6}$ 15 nm are realized in order to more easily characterize the nanoribbon dimensions. Both  $R_l$  and  $R_w$  increase superlinearly with  $x_{CH_4}$ . To extract the rate laws, the data in Figure 4a,b are plotted on a log-log scale (Figure 4a,b inset), and the slope of the linear fit is computed. Over the range of  $x_{CH_4}$  measured,  $R_l$ empirically scales as  $x_{\rm CH_4}^{2.8}$  and  $R_{\rm w}$  scales as  $x_{\rm CH_4}^{3.8}$ . Figure 4c shows a plot of aspect ratio (l/w) versus  $x_{CH_4}$ . As expected from the rate laws,  $R_{\omega}$  increases at a much faster rate than  $R_{l}$  as  $x_{\rm CH_a}$  is increased, resulting in a decay of the average aspect ratio from 29  $\pm$  11 to 12  $\pm$  3. These data underscore the importance of  $x_{CH_4}$  in controlling the aspect ratio of graphene nanoribbons and in conducting synthesis at low  $R_l$  in order to obtain high l/w.

Surface Roughness Due to Nanoribbon Synthesis. Surface roughening of the Ge(001) surface during graphene nanoribbon synthesis has been previously reported<sup>22</sup> and can potentially affect the carrier mobility of nanoribbons on Ge by increasing surface scattering. Therefore, we next study the impact of nanoribbon synthesis on the surface roughness of Ge/Si(001) and Ge(001). We find that the roughness depends on (1) the density of the nanoribbons and (2) the length of the nanoribbons. These two variables are decoupled and separately studied in Figure 5.

Figure 5a shows a plot of post-growth rms roughness of the surface versus the density of nanoribbons for a fixed t = 3 h and  $x_{\rm CH_4} = 6.6 \times 10^{-3}$ . The density is tuned by varying the duration of the pregrowth annealing time from 0 to 30 min, in which longer annealing leads to a lower nucleation density. Note that the duration of the annealing itself does not impact the roughness (Figure 1d,e) but rather reduces the density of absorbates (or potential nucleation sites) on the surface. The rms roughness is computed over several 10  $\mu$ m  $\times$  10  $\mu$ m regions of each sample. The rms roughness for both Ge/ Si(001) and Ge(001) follows indistinguishable trends and values with increasing nanoribbon density. The dashed red and blue lines represent rms roughness for Ge/Si(001) and Ge(001), respectively, when no CH<sub>4</sub> is flowed for the entire duration (t = 3 h) of the synthesis, which results in a nucleation density of 0. If CH<sub>4</sub> is not flowed, the rms roughness remains <1 nm. In contrast, the nucleation and growth of nanoribbons at a density of 100  $\mu m^{-2}$  increase the rms roughness to >5 nm on both Ge/Si(001) and Ge(001) substrates.

Increasing the length and width of the nanoribbons at fixed nanoribbon density also leads to surface roughening. In Figure 5b, the growth time, t, is varied using a constant pregrowth annealing time of 30 min and  $\alpha_{\rm CH_4} = 6.6 \times 10^{-3}$ . The nucleation density at these fixed conditions varies only by a factor of 4  $(0.5-2~\mu{\rm m}^{-2})$  versus a factor of >100 when the pregrowth annealing time is varied, as in Figure 5a. The rms roughness of the surface increases continuously with t (or l or w), for example, increasing from 1.6 to 8.3 nm, as the average nanoribbon length increases from 130 to 960 nm and average nanoribbon width increases from 10 to 45 nm in Figure 5b.

The roughening of both the Ge/Si(001) and Ge(001) surfaces is likely driven by the tendency of Ge to locally form nanofacets underneath the nanoribbons.<sup>22</sup> At the same time,

The Journal of Physical Chemistry C

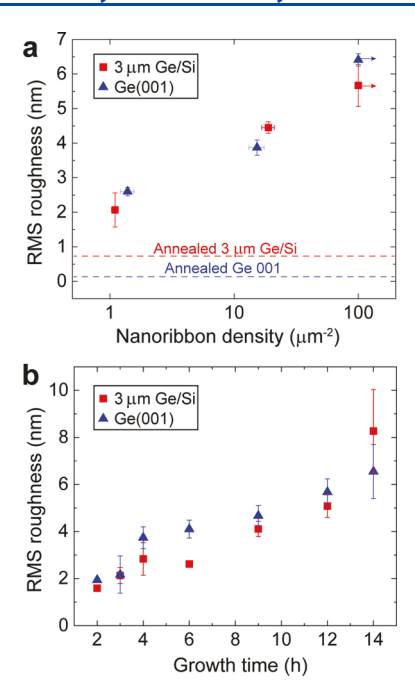


Figure 5. (a) Plot of rms roughness of Ge/Si(001) and Ge(001) surfaces vs nanoribbon density for growth at 910 °C, t = 3 h, and  $x_{\rm CH_4} = 6.6 \times 10^{-3}$ . Nanoribbon density is tuned by varying the pregrowth annealing time from 0 to 30 min. Dotted lines correspond to the surface roughness on substrates on which nanoribbons are not nucleated. The arrows attached to the data points at a nanoribbon density of  $100~\mu{\rm m}^{-2}$  indicate that the measured nanoribbon density is a lower bound for the actual nanoribbon density. At high densities, the nanoribbons sometimes merge together, complicating quantification of the densities. (b) Plot of rms roughness vs growth time for approximately the same nanoribbon density  $(0.5-2~\mu{\rm m}^{-2})$ ,  $x_{\rm CH_4} = 6.6 \times 10^{-3}$ , and growth temperature = 910 °C.

the presence of the nanoribbons locally modulates the sublimation rate of Ge. In regions of the substrate not passivated by nanoribbons, there is continuous sublimation of Ge, leading to valleys, whereas in regions passivated by nanoribbons, the sublimation of Ge is suppressed, leading to hills (Figures S6 and S7).<sup>22</sup>

**Silicon Diffusion to the Surface during Nanoribbon Growth.** For graphene growth on Ge/Si(001), an important consideration is Si diffusion from the bulk substrate into the Ge epilayer. Diffusion of Si to the surface can lead to the formation of SiC in the presence of CH<sub>4</sub> at temperatures >800 °C. <sup>40</sup> This problem is more pronounced in the case of graphene nanoribbon synthesis because higher growth temperatures (>860 °C) and slower growth rates (and thus longer growth times) are required to obtain high aspect nanoribbons with sub-10 nm widths that have a technologically relevant band gap, thereby increasing the total thermal budget of the processing.

To gain further insight into the diffusion of Si to the Ge surface, XPS is used to quantify the Ge/Si composition of the epilayer surface after various growth times, and SEM and Raman spectroscopy are used to spatially map the surface. All growths are conducted at 910 °C with a 30 min annealing time and  $x_{\rm CH_4} = 6.6 \times 10^{-3}$ . XPS spectra are collected and averaged from five random locations on the substrate, each with a spot size of 400  $\mu$ m.

Figure 6a shows the surface atomic fraction ratio of Ge/Si versus growth time (t). Prior to annealing and nanoribbon

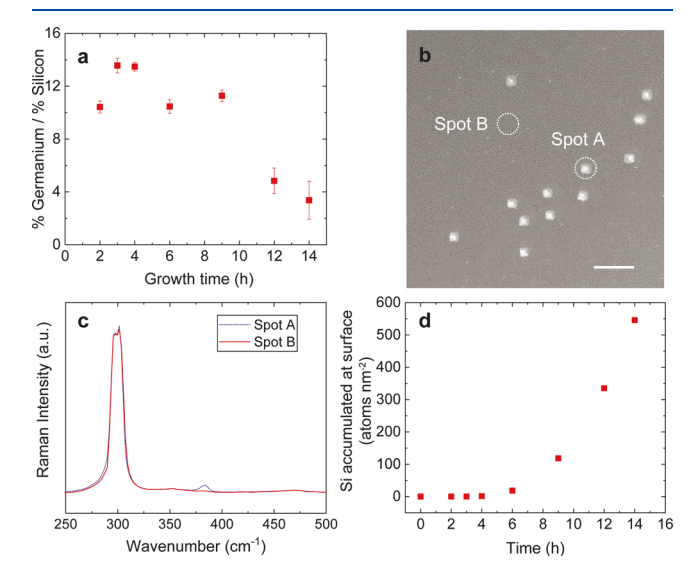


**Figure 6.** Silicon diffusion to the surface of Ge/Si(001). (a) Plot of Ge/Si ratio at the surface vs growth time. (b) SEM micrograph of the Ge/Si(001) surface after t=12 h. (c) Raman spectra at spots A and B, as highlighted in (b). All growths are conducted at 910 °C with  $x_{\rm CH_4}=6.6\times10^{-3}$ . (d) Plot of Si accumulated at the surface vs time—assuming the worst case in which all Si atoms that diffuse to the surface are sinked there—simulated using Ge–Si interdiffusion coefficients. Scale bar in (b) is 10  $\mu$ m.

synthesis, there is no detectable Si on the surface (i.e., Ge/Si is ∞). Ge/Si immediately reduces to 12 upon initiating nanoribbon synthesis but remains relatively constant for t <9 h. This initial temporal invariance indicates that the pathway for Si diffusion to the surface at short t < 9 h is mediated by local defects or flaws in the Ge epilayer (e.g., threading dislocations<sup>72</sup> or stacking faults<sup>73</sup>) because the relatively slower Si diffusion from bulk to the surface would lead to a monotonic decrease in Ge/Si with time. It is not yet clear if these defects or flaws originate from the Ge epitaxial growth process or if they form when the substrate temperature is elevated to 910 °C for the pregrowth annealing and nanoribbon synthesis.<sup>74</sup> Examples of features on the surface that may indicate local Si accumulation are shown in Figure S8. These features appear bright in the SEM and can range from 50 nm to 20  $\mu$ m in lateral size and have been observed previously.<sup>28</sup> Away from these features, the nanoribbon synthesis is not perturbed (Figures 2, 3, and S8b).

For t > 9 h, the surface Ge/Si ratio begins to monotonically decrease, falling <5 for t > 12 h, concurrent with appearance of hillocks that appear bright, as shown in Figure 6b. Such hillocks have been observed in previous studies of annealed SiGe/Si(001) substrates and are attributed to intermixing of Si and Ge. To confirm that these hillocks are related to Si diffusion to the surface, Raman spectra are obtained (Figure 6c) over regions with and without hillocks (spot A and spot B in Figure 6b, respectively). Regions with hillocks display a peak at 380 cm<sup>-1</sup>, characteristic of SiGe, whereas this peak is absent in the regions without hillocks. The size and density of the hillocks also increase with time for t > 12 h, as shown in Figure S9, indicating increased diffusion of Si to the surface. At t = 18 h, the surface is fully covered by hillocks, but

nanoribbons can be clearly seen atop these hillocks (Figure S8c).

A diffusion model is used to analyze the flux of Si reaching the Ge surface using previously measured composition and temperature-dependent diffusion coefficients<sup>77</sup> and assuming an extreme scenario that all Si reaching the surface is sinked as SiC, SiO<sub>x</sub>C<sub>y</sub>, and SiO<sub>2</sub> and therefore accumulates on the surface (see Figure S10). The calculated total Si accumulating at the surface versus time in this extreme scenario is shown in Figure 6d and is 1.5, 18.5, 335, and 546 atoms nm<sup>-2</sup> for t = 4, 6, 12, and 14 h, respectively. Thus, the decrease in the surface Ge/Si ratio for t > 9 h can be attributed to the enhanced diffusive flux of Si to the surface that occurs for later times.

These experimental data indicate that in order to synthesize graphene nanoribbons on a 3  $\mu$ m Ge epilayer on Si(001) at 910 °C and prevent bulk Si diffusion to the surface, growth times must be limited to less than 9 h. Furthermore, improving the quality of the Ge epilayer to minimize defects and flaws will be important to eliminate Si surface features at shorter growth times.

To reinforce that the starting surface must be relatively Sifree in order to maintain low surface roughness, prevent SiC formation, and achieve pristine graphene growth, we attempt to synthesize graphene on Si<sub>0.15</sub>Ge<sub>0.85</sub>(111) sputtered on *c*-sapphire using a published procedure. Figure S1a shows a SEM micrograph of the surface after CVD at 960 °C. The surface appears rough and is interspersed with white particles, which presumably are SiC. XPS confirms a significant presence of SiC (Figure S1b), and although Raman spectra at the surface indicate that graphene is synthesized (Figure S1d), it is highly defective, as revealed by a large D-band Raman mode that is stronger than the G-band Raman mode of graphene. 80

Role of Threading Dislocations on Nanoribbon Growth. Because threading dislocations are inevitably present in Ge/Si(001) due to the 4.2% lattice mismatch between Ge and Si,81 an important question to ask is does their presence or location influence the nucleation or growth of nanoribbons? To answer this question, graphene nanoribbons on Ge/ Si(001) at 910 °C are synthesized with  $x_{\rm CH_a} = 8.3 \times 10^{-3}$  for t = 2.4 h and imaged via SEM (Figure S11a). The substrate is then etched in SECCO solution for 1 min, producing etch pits that reveal the location of the threading dislocations, and is imaged again via SEM. The same region of the sample, before and after the SECCO etch, is identified with the aid of Au markers on the sample (Figure S11b). The pre- and post-SECCO etch images are next false-colored and superimposed to generate a composite image (Figure 7). More composite images can be found in Figure S12. The graphene nanoribbons are shown in red, whereas the etch pits that reveal the location of the dislocations are shown in blue. It is evident that nanoribbons nucleate and grow both on regions with and without threading dislocations, without a change in aspect ratio or growth rate. This insensitivity to threading dislocations is conceivable because graphene nanoribbons readily grow over steps and terraces on Ge(001)<sup>22</sup> and threading dislocations terminate as bilayer steps on the Ge/Si(001) surface. 82,83

### CONCLUSIONS

In this study, we demonstrate graphene nanoribbon synthesis on low TDD, CMOS-compatible Ge/Si(001), using CVD. These nanoribbons, similar to ones on Ge(001), are self-

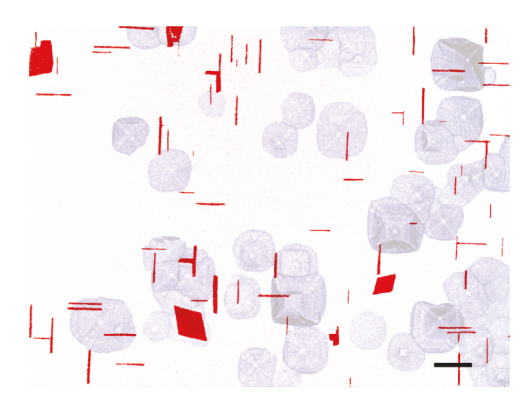


Figure 7. Superimposed image of graphene nanoribbons (red) and etch pits (blue) located at threading dislocations formed after SECCO etch. Scale bar is 1  $\mu$ m.

defining and oriented toward Ge(110) directions. By tuning the partial pressure of CH<sub>4</sub>, highly anisotropic nanoribbons with aspect ratio as high as 50 are obtained. Using STM, we reveal that these nanoribbons can have sub-10 nm widths and smooth armchair edges with an edge roughness of  $1a_0$  or less over a length of 10 nm, both of which are essential for future technology. Moreover, graphene nanoribbons on Ge/Si(001) follow identical growth evolution and kinetics as on Ge(001). We show that surface roughness follows indistinguishable trends on both substrates, suggesting that surface topology is affected only by nanoribbon growth and is insensitive to the bulk constituents of the substrates. For t < 9 h, surface Si is invariably constant and likely originates via imperfections formed during epitaxial Ge growth on Si. On the contrary, for t > 9 h, surface Si increases monotonically, resulting in the appearance of SiGe hillocks. We also show that the starting surface must be relatively Si-free to prevent SiC formation. Finally, we conclude that neither nanoribbon nucleation nor growth is influenced by the presence of threading dislocations.

These data are important because they show that Ge epilayers afford the synthesis of graphene nanoribbons on Si wafer platforms. A 3  $\mu$ m epilayer sufficiently suppresses Si diffusion to the Ge surface for an extended enough duration to afford 9 h of synthesis, which is more than enough time to grow high-quality nanoribbons. For example, 3 h of synthesis at  $x_{\rm CH_4} = 6.6 \times 10^{-3}$  is sufficient to yield nanoribbons that are 5 nm wide and 200 nm long (Figure 2d). Moreover, the data show that all previous work on the nanoribbon synthesis on Ge(001) can be replicated on Ge/Si(001) and that threading dislocations (which will be prevalent in all Ge epilayers) are not problematic for nanoribbon synthesis. Subsequently, the selective etching of Ge over Si could provide a route for integrating spatially patterned islands of semiconducting graphene on Ge or for relaxing nanoribbons directly onto Si or SiO<sub>2</sub> surfaces, enabling hybrid C/Ge/Si or C/Si electronics. Overall, these data provide strong motivation for further research into the potential of Ge/Si(001) as a platform for the wafer-scale synthesis of semiconducting graphene.

# METHODS

Nanoribbon Synthesis. Ge/Si(001) (3  $\mu$ m) and Si<sub>0.15</sub>Ge<sub>0.85</sub> (111) (fabricated using published procedures <sup>55,78</sup>) and undoped Ge(001) (purchased from Wafer World, part #1459) substrates were loaded into a horizontal quartz tube furnace in which the furnace can slide over the length of the

tube. Prior to nanoribbon synthesis, the CVD chamber was evacuated to  $<\!10^{-2}$  Torr using a scroll pump. The system was then back-filled with Ar and  $H_2$ , and a steady flow (200 sccm Ar, 100 sccm  $H_2$ ) monitored by mass flow controllers was maintained at ambient pressure. The furnace was then slid to surround the samples, and annealing was performed for the requisite duration. To initiate the nanoribbon growth,  $CH_4$  was introduced for the required duration. To terminate the growth, the furnace was slid away from the samples, and the portion of the quartz tube containing the samples was cooled to room temperature.

**Characterization.** After the nanoribbon synthesis, samples were characterized using SEM (LEO-1530) at 5 kV and AFM (Veeco MultiMode SPM) in tapping mode. For XRD (PANalytical Empyrean), high-resolution  $\omega$ –2 $\theta$  scans around the (004) reflection were obtained using monochromatic Cu  $K\alpha$  ( $\lambda = 1.5406$  Å; 40 kV; 40 mA). Surface XPS spectra were acquired using a Thermo K-Alpha XPS with a spot size of 400  $\mu$ m and monochromatic Al K $\alpha$  radiation (1486.7 eV). Survey and individual spectra were acquired using analyzer pass energies of 188 and 50 eV, respectively, with a resolution of 0.1 eV and a collection time of 50 ms. Depth profile etches were performed using an in situ Ar<sup>+</sup> ion gun (3000 eV, 3.25 A). The etch rate of the ion gun for Ge was calibrated to be  $0.1 \text{ nm s}^{-1}$ . STM and STS (Omicron VT, base pressure of  $5 \times 10^{-11}$  mbar) were simultaneously performed at either 300 or 55 K using electrochemically etched W tips. STS data were generated by superimposing a 30 mV modulation at 10 kHz on top of the bias voltage and analyzing the tunneling current with a SR830 lock-in amplifier.

#### ASSOCIATED CONTENT

## **S** Supporting Information

The Supporting Information is available free of charge on the ACS Publications website at DOI: 10.1021/acs.jpcc.9b04390.

Characterization of the  $\mathrm{Si}_{0.15}\mathrm{Ge}_{0.85}$  surface after CVD; EBSD of Ge/Si(001) and Ge(001); additional STM data and figures and point STS; SEM of calibration carbon nanotubes on Ge(001); AFM of graphene nanoribbons on Ge/Si(001) with varying densities and lengths; additional experimental and modeling data of silicon diffusion in Ge/Si(001); and pre- and post-SECCO etch images (PDF)

## AUTHOR INFORMATION

# **Corresponding Author**

\*E-mail: michael.arnold@wisc.edu.

ORCID ®

Vivek Saraswat: 0000-0001-5095-3078

Robert M. Jacobberger: 0000-0001-5947-5308 Katherine R. Jinkins: 0000-0001-5757-1136 Austin J. Way: 0000-0002-7418-8590 Nathan P. Guisinger: 0000-0001-7437-2331

**Notes** 

The authors declare no competing financial interest.

#### ACKNOWLEDGMENTS

We thank Donald E. Savage for help with XRD measurements. We are grateful to Thomas Jones and William Humphreys at NASA Langley Research Center for critiquing the manuscript. This research is primarily supported by the U.S. Department of

Energy, Office of Science, Basic Energy Sciences, under award no. DE-SC0016007 (V.S., R.M.J., A.J.W., and M.S.A.) for graphene growth experiments and characterization via SEM, Raman, XPS, XRD, and AFM. Partial support is also acknowledged from the National Science Foundation (NSF) via SNM-IS award no. 1727523 (K.R.J. and M.S.A.) for SEM resolution calibration experiments. This work was performed, in part, at the Center for Nanoscale Materials, a U.S. Department of Energy Office of Science User Facility, and supported by the U.S. Department of Energy, Office of Science, under contract no. DE-AC02-06CH11357. The STM characterization was performed at the Center for Nanoscale Materials. K.R.J. also acknowledges support from the NSF Graduate Research Fellowship Program under award no. DGE-1256259. The authors acknowledge the use of facilities and instrumentation supported by the NSF through the University of Wisconsin Materials Research Science and Engineering Center (grant no. DMR-1720415)

# REFERENCES

- (1) Fang, T.; Konar, A.; Xing, H.; Jena, D. Mobility in Semiconducting Graphene Nanoribbons: Phonon, Impurity, and Edge Roughness Scattering. *Phys. Rev. B: Condens. Matter Mater. Phys.* **2008**, 78, 205403.
- (2) Baringhaus, J.; Ruan, M.; Edler, F.; Tejeda, A.; Sicot, M.; Taleb-Ibrahimi, A.; Li, A.-P.; Jiang, Z.; Conrad, E. H.; Berger, C.; et al. Exceptional Ballistic Transport in Epitaxial Graphene Nanoribbons. *Nature* **2014**, *506*, 349–354.
- (3) Liao, A. D.; Wu, J. Z.; Wang, X. R.; Tahy, K.; Jena, D.; Dai, H. J.; Pop, E. Thermally Limited Current Carrying Ability of Graphene Nanoribbons. *Phys. Rev. Lett.* **2011**, *106*, 256801.
- (4) Son, Y.-W.; Cohen, M. L.; Louie, S. G. Energy gaps in graphene nanoribbons. *Phys. Rev. Lett.* **2006**, *97*, 216803.
- (5) Yang, L.; Park, C. H.; Son, Y. W.; Cohen, M. L.; Louie, S. G. Quasiparticle Energies and Band Gaps in Graphene Nanoribbons. *Phys. Rev. Lett.* **2007**, *99*, 186801.
- (6) Schwierz, F. Graphene Transistors. Nat. Nanotechnol. 2010, 5, 487-496.
- (7) Zeng, M.; Xiao, Y.; Liu, J.; Lu, W.; Fu, L. Controllable Fabrication of Nanostructured Graphene Towards Electronics. *Adv. Electron. Mater.* **2016**, *2*, 1500456.
- (8) Liao, L.; Bai, J.; Lin, Y.-C.; Qu, Y.; Huang, Y.; Duan, X. High-Performance Top-Gated Graphene-Nanoribbon Transistors Using Zirconium Oxide Nanowires As High-Dielectric-Constant Gate Dielectrics. *Adv. Mater.* **2010**, *22*, 1941–1945.
- (9) Lin, Y.-M.; Jenkins, K. A.; Valdes-Garcia, A.; Small, J. P.; Farmer, D. B.; Avouris, P. Operation of Graphene Transistors at Gigahertz Frequencies. *Nano Lett.* **2009**, *9*, 422–426.
- (10) Anwar, F.; Carlos, C. R.; Saraswat, V.; Mangu, V. S.; Arnold, M. S.; Cavallo, F. Nanoscale Graphene/Ge Wigglers As Building Blocks for THz Sources. *AIP Adv.* **2017**, *7*, 115015.
- (11) Abbas, A. N.; Liu, G.; Liu, B.; Zhang, L.; Liu, H.; Ohlberg, D.; Wu, W.; Zhou, C. Patterning, Characterization, and Chemical Sensing Applications of Graphene Nanoribbon Arrays Down to 5 nm Using Helium Ion Beam Lithography. ACS Nano 2014, 8, 1538–1546.
- (12) Huang, B.; Li, Z.; Liu, Z.; Zhou, G.; Hao, S.; Wu, J.; Gu, B.-L.; Duan, W. Adsorption of Gas Molecules on Graphene Nanoribbons and Its Implication for Nanoscale Molecule Sensor. *J. Phys. Chem. C* **2008**, *112*, 13442–13446.
- (13) Han, M. Y.; Ozyilmaz, B.; Zhang, Y. B.; Kim, P. Energy Band-Gap Engineering of Graphene Nanoribbons. *Phys. Rev. Lett.* **2007**, 98, 206805.
- (14) Li, X.; Wang, X.; Zhang, L.; Lee, S.; Dai, H. Chemically Derived, Ultrasmooth Graphene Nanoribbon Semiconductors. *Science* **2008**, *319*, 1229–1232.
- (15) Kosynkin, D. V.; Higginbotham, A. L.; Sinitskii, A.; Lomeda, J. R.; Dimiev, A.; Price, B. K.; Tour, J. M. Longitudinal Unzipping of

- Carbon Nanotubes to Form Graphene Nanoribbons. *Nature* **2009**, 458, 872–876.
- (16) Vo, T. H.; Shekhirev, M.; Kunkel, D. A.; Morton, M. D.; Berglund, E.; Kong, L. M.; Wilson, P. M.; Dowben, P. A.; Enders, A.; Sinitskii, A. Large-Scale Solution Synthesis of Narrow Graphene Nanoribbons. *Nat. Commun.* **2014**, *5*, 3189.
- (17) Narita, A.; Feng, X.; Hernandez, Y.; Jensen, S. A.; Bonn, M.; Yang, H.; Verzhbitskiy, I. A.; Casiraghi, C.; Hansen, M. R.; Koch, A. H. R.; et al. Synthesis of Structurally Well-Defined and Liquid-Phase-Processable Graphene Nanoribbons. *Nat. Chem.* **2014**, *6*, 126–132.
- (18) Cai, J.; Ruffieux, P.; Jaafar, R.; Bieri, M.; Braun, T.; Blankenburg, S.; Muoth, M.; Seitsonen, A. P.; Saleh, M.; Feng, X.; et al. Atomically Precise Bottom-Up Fabrication of Graphene Nanoribbons. *Nature* **2010**, *466*, 470–473.
- (19) Huang, H.; Wei, D. C.; Sun, J. T.; Wong, S. L.; Feng, Y. P.; Castro Neto, A. H.; Wee, A. T. S. Spatially Resolved Electronic Structures of Atomically Precise Armchair Graphene Nanoribbons. *Sci. Rep.* **2012**, *2*, 983.
- (20) Narita, A.; Chen, Z.; Chen, Q.; Müllen, K. Solution and On-Surface Synthesis of Structurally Defined Graphene Nanoribbons as a New Family of Semiconductors. *Chem. Sci.* **2019**, *10*, 964–975.
- (21) Sprinkle, M.; Ruan, M.; Hu, Y.; Hankinson, J.; Rubio-Roy, M.; Zhang, B.; Wu, X.; Berger, C.; de Heer, W. A. Scalable Templated Growth of Graphene Nanoribbons on SiC. *Nat. Nanotechnol.* **2010**, *5*, 727–731.
- (22) Jacobberger, R. M.; Kiraly, B.; Fortin-Deschenes, M.; Levesque, P. L.; McElhinny, K. M.; Brady, G. J.; Delgado, R. R.; Roy, S. S.; Mannix, A.; Lagally, M. G.; et al. Direct Oriented Growth of Armchair Graphene Nanoribbons on Germanium. *Nat. Commun.* **2015**, *6*, 8006.
- (23) Jacobberger, R. M.; Murray, E. A.; Fortin-Deschênes, M.; Göltl, F.; Behn, W. A.; Krebs, Z. J.; Levesque, P. L.; Savage, D. E.; Smoot, C.; Lagally, M. G.; et al. Alignment of Semiconducting Graphene Nanoribbons on Vicinal Ge(001). *Nanoscale* **2019**, *11*, 4864–4875.
- (24) Way, A. J.; Jacobberger, R. M.; Arnold, M. S. Seed-Initiated Anisotropic Growth of Unidirectional Armchair Graphene Nanoribbon Arrays on Germanium. *Nano Lett.* **2018**, *18*, 898–906.
- (25) Kiraly, B.; Mannix, A. J.; Jacobberger, R. M.; Fisher, B. L.; Arnold, M. S.; Hersam, M. C.; Guisinger, N. P. Sub-5 nm, Globally Aligned Graphene Nanoribbons on Ge(001). *Appl. Phys. Lett.* **2016**, *108*, 213101.
- (26) Scaparro, A. M.; Miseikis, V.; Coletti, C.; Notargiacomo, A.; Pea, M.; De Seta, M.; Di Gaspare, L. Investigating the CVD Synthesis of Graphene on Ge(100): Toward Layer-by-Layer Growth. *ACS Appl. Mater. Interfaces* **2016**, *8*, 33083–33090.
- (27) Di Gaspare, L.; Scaparro, A. M.; Fanfoni, M.; Fazi, L.; Sgarlata, A.; Notargiacomo, A.; Miseikis, V.; Coletti, C.; De Seta, M. Early Stage of CVD Graphene Synthesis on Ge(001) Substrate. *Carbon* **2018**, *134*, 183–188.
- (28) Dabrowski, J.; Lippert, G.; Avila, J.; Baringhaus, J.; Colambo, I.; Dedkov, Y. S.; Herziger, F.; Lupina, G.; Maultzsch, J.; Schaffus, T.; et al. Understanding the Growth Mechanism of Graphene on Ge/Si(001) Surfaces. Sci. Rep. 2016, 6, 31639.
- (29) Pasternak, I.; Dabrowski, P.; Ciepielewski, P.; Kolkovsky, V.; Klusek, Z.; Baranowski, J. M.; Strupinski, W. Large-Area High-Quality Graphene on Ge(001)/Si(001) Substrates. *Nanoscale* **2016**, *8*, 11241–11247.
- (30) Lee, J.-H.; Lee, E. K.; Joo, W.-J.; Jang, Y.; Kim, B.-S.; Lim, J. Y.; Choi, S.-H.; Ahn, S. J.; Ahn, J. R.; Park, M.-H.; et al. Wafer-Scale Growth of Single-Crystal Monolayer Graphene on Reusable Hydrogen-Terminated Germanium. *Science* 2014, 344, 286–289.
- (31) Pasternak, I.; Wesolowski, M.; Jozwik, I.; Lukosius, M.; Lupina, G.; Dabrowski, P.; Baranowski, J. M.; Strupinski, W. Graphene Growth on Ge(100)/Si(100) Substrates by CVD Method. *Sci. Rep.* **2016**, *6*, 21773.
- (32) Lukosius, M.; Dabrowski, J.; Kitzmann, J.; Fursenko, O.; Akhtar, F.; Lisker, M.; Lippert, G.; Schulze, S.; Yamamoto, Y.; Schubert, M. A.; et al. Metal-Free CVD Graphene Synthesis on 200 mm Ge/Si(001) Substrates. ACS Appl. Mater. Interfaces 2016, 8, 33786–33793.

- (33) Wang, G.; Zhang, M.; Zhu, Y.; Ding, G. Q.; Jiang, D.; Guo, Q. L.; Liu, S.; Xie, X. M.; Chu, P. K.; Di, Z. F.; et al. Direct Growth of Graphene Film on Germanium Substrate. *Sci. Rep.* **2013**, *3*, 2465.
- (34) Jacobberger, R. M.; Arnold, M. S. High-Performance Charge Transport in Semiconducting Armchair Graphene Nanoribbons Grown Directly on Germanium. *ACS Nano* **2017**, *11*, 8924–8929.
- (35) Kiraly, B.; Jacobberger, R. M.; Mannix, A. J.; Campbell, G. P.; Bedzyk, M. J.; Arnold, M. S.; Hersam, M. C.; Guisinger, N. P. Electronic and Mechanical Properties of Graphene-Germanium Interfaces Grown by Chemical Vapor Deposition. *Nano Lett.* **2015**, 15, 7414–7420.
- (36) McElhinny, K. M.; Jacobberger, R. M.; Zaug, A. J.; Arnold, M. S.; Evans, P. G. Graphene-Induced Ge (001) Surface Faceting. *Surf. Sci.* **2016**, *647*, 90–95.
- (37) Persichetti, L.; Di Gaspare, L.; Fabbri, F.; Scaparro, A. M.; Notargiacomo, A.; Sgarlata, A.; Fanfoni, M.; Miseikis, V.; Coletti, C.; De Seta, M. Abrupt Changes in the Graphene on Ge(001) System at the Onset of Surface Melting. *Carbon* **2019**, *145*, 345–351.
- (38) Fisher, G.; Seacrist, M. R.; Standley, R. W. Silicon Crystal Growth and Wafer Technologies. *Proc. IEEE* **2012**, *100*, 1454–1474.
- (39) Vanhellemont, J.; Simoen, E. Brother Silicon, Sister Germanium. J. Electrochem. Soc. 2007, 154, H572-H583.
- (40) Trung, P. T.; Campos-Delgado, J.; Joucken, F.; Colomer, J. F.; Hackens, B.; Raskin, J. P.; Santos, C. N.; Robert, S. Direct Growth of Graphene on Si(111). *J. Appl. Phys.* **2014**, *115*, 223704.
- (41) Chen, Y.; Gong, X.-L.; Gai, J.-G. Progress and Challenges in Transfer of Large-Area Graphene Films. Adv. Sci. 2016, 3, 1500343.
- (42) Bautista-Flores, C.; Sato-Berru, R. Y.; Mendoza, D. Raman Spectroscopy of CVD Graphene During Transfer Process From Copper to SiO<sub>2</sub>/Si Substrates. *Mater. Res. Express* **2018**, *6*, 015601.
- (43) Hallam, T.; Berner, N. C.; Yim, C.; Duesberg, G. S. Strain, Bubbles, Dirt, and Folds: A Study of Graphene Polymer-Assisted Transfer. *Adv. Mater. Interfaces* **2014**, *1*, 1400115.
- (44) Pirkle, A.; Chan, J.; Venugopal, A.; Hinojos, D.; Magnuson, C. W.; McDonnell, S.; Colombo, L.; Vogel, E. M.; Ruoff, R. S.; Wallace, R. M. The Effect of Chemical Residues on the Physical and Electrical Properties of Chemical Vapor Deposited Graphene Transferred to SiO<sub>2</sub>. Appl. Phys. Lett. **2011**, 99, 122108.
- (45) Lupina, G.; Kitzmann, J.; Costina, I.; Lukosius, M.; Wenger, C.; Wolff, A.; Vaziri, S.; Östling, M.; Pasternak, I.; Krajewska, A.; et al. Residual Metallic Contamination of Transferred Chemical Vapor Deposited Graphene. *ACS Nano* **2015**, *9*, 4776–4785.
- (46) Linden, S.; Zhong, D.; Timmer, A.; Aghdassi, N.; Franke, J. H.; Zhang, H.; Feng, X.; Mullen, K.; Fuchs, H.; Chi, L.; et al. Electronic Structure of Spatially Aligned Graphene Nanoribbons on Au(788). *Phys. Rev. Lett.* **2012**, *108*, 216801.
- (47) Senkovskiy, B. V.; Pfeiffer, M.; Alavi, S. K.; Bliesener, A.; Zhu, J.; Michel, S.; Fedorov, A. V.; German, R.; Hertel, D.; Haberer, D.; et al. Making Graphene Nanoribbons Photoluminescent. *Nano Lett.* **2017**, *17*, 4029–4037.
- (48) Chen, Z.; Zhang, W.; Palma, C.-A.; Lodi Rizzini, A.; Liu, B.; Abbas, A.; Richter, N.; Martini, L.; Wang, X.-Y.; Cavani, N.; et al. Synthesis of Graphene Nanoribbons by Ambient-Pressure Chemical Vapor Deposition and Device Integration. *J. Am. Chem. Soc.* **2016**, 138, 15488–15496.
- (49) Wang, D. B.; Tian, H.; Yang, Y.; Xie, D.; Ren, T. L.; Zhang, Y. G. Scalable and Direct Growth of Graphene Micro Ribbons on Dielectric Substrates. *Sci. Rep.* **2013**, *3*, 1348.
- (50) de Oteyza, D. G.; García-Lekue, A.; Vilas-Varela, M.; Merino-Díez, N.; Carbonell-Sanromà, E.; Corso, M.; Vasseur, G.; Rogero, C.; Guitián, E.; Pascual, J. I.; et al. Substrate-Independent Growth of Atomically Precise Chiral Graphene Nanoribbons. *ACS Nano* **2016**, *10*, 9000–9008.
- (51) Fairbrother, A.; Sanchez-Valencia, J.-R.; Lauber, B.; Shorubalko, I.; Ruffieux, P.; Hintermann, T.; Fasel, R. High Vacuum Synthesis and Ambient Stability of Bottom-Up Graphene Nanoribbons. *Nanoscale* **2017**, *9*, 2785–2792.

- (52) Kato, T.; Hatakeyama, R. Site- and Alignment-Controlled Growth of Graphene Nanoribbons From Nickel Nanobars. *Nat. Nanotechnol.* **2012**, *7*, 651–656.
- (53) Suzuki, H.; Kaneko, T.; Shibuta, Y.; Ohno, M.; Maekawa, Y.; Kato, T. Wafer-Scale Fabrication and Growth Dynamics of Suspended Graphene Nanoribbon Arrays. *Nat. Commun.* **2016**, *7*, 11797.
- (54) Lippert, G.; Dąbrowski, J.; Schroeder, T.; Schubert, M. A.; Yamamoto, Y.; Herziger, F.; Maultzsch, J.; Baringhaus, J.; Tegenkamp, C.; Asensio, M. C.; et al. Graphene Grown on Ge(001) From Atomic Source. *Carbon* **2014**, *75*, 104–112.
- (55) Yamamoto, Y.; Zaumseil, P.; Schubert, M. A.; Tillack, B. Influence of Annealing Conditions on Threading Dislocation Density in Ge Deposited on Si by Reduced Pressure Chemical Vapor Deposition. Semicond. Sci. Technol. 2018, 33, 124007.
- (56) Yamamoto, Y.; Zaumseil, P.; Arguirov, T.; Kittler, M.; Tillack, B. Low Threading Dislocation Density Ge Deposited on Si (100) using RPCVD. *Solid-State Electron.* **2011**, *60*, 2–6.
- (57) Hartmann, J. M.; Aubin, J. Assessment of the Growth/Etch Back Technique for the Production of Ge Strain-Relaxed Buffers on Si. J. Cryst. Growth 2018, 488, 43–50.
- (58) Abbadie, A.; Allibert, F.; Brunier, F. Defect Delineation and Characterization in SiGe, Ge and Other Semiconductor-on-Insulator Structures. *Solid-State Electron.* **2009**, *53*, 850–857.
- (59) Bogumilowicz, Y.; Hartmann, J. M.; Truche, R.; Campidelli, Y.; Rolland, G.; Billon, T. Chemical Vapour Etching of Si, SiGe and Ge with HCl; Applications to the Formation of Thin Relaxed SiGe Buffers and to the Revelation of Threading Dislocations. *Semicond. Sci. Technol.* **2005**, 20, 127–134.
- (60) Abbadie, A.; Bedell, S. W.; Hartmann, J. M.; Sadana, D. K.; Brunier, F.; Figuet, C.; Cayrefourcq, I. Study of HCl and Secco Defect Etching for Characterization of Thick SSOI. *J. Electrochem. Soc.* **2007**, *154*, H713—H719.
- (61) Yamamoto, Y.; Kozlowski, G.; Zaumseil, P.; Tillack, B. Low Threading Dislocation Ge on Si by Combining Deposition and Etching. *Thin Solid Films* **2012**, *520*, 3216–3221.
- (62) Loo, R.; Wang, G.; Souriau, L.; Lin, J. C.; Takeuchi, S.; Brammertz, G.; Caymax, M. High Quality Ge Virtual Substrates on Si Wafers with Standard STI Patterning. *J. Electrochem. Soc.* **2010**, *157*, H13—H21
- (63) Lauffer, P.; Emtsev, K. V.; Graupner, R.; Seyller, T.; Ley, L.; Reshanov, S. A.; Weber, H. B. Atomic and Electronic Structure of Few-Layer Graphene on SiC(0001) Studied With Scanning Tunneling Microscopy and Spectroscopy. *Phys. Rev. B: Condens. Matter Mater. Phys.* **2008**, 77, 155426.
- (64) Rutter, G. M.; Guisinger, N. P.; Crain, J. N.; Jarvis, E. A. A.; Stiles, M. D.; Li, T.; First, P. N.; Stroscio, J. A. Imaging the Interface of Epitaxial Graphene With Silicon Carbide via Scanning Tunneling Microscopy. *Phys. Rev. B: Condens. Matter Mater. Phys.* **2007**, 76, 235416
- (65) Yang, H.; Mayne, A. J.; Boucherit, M.; Comtet, G.; Dujardin, G.; Kuk, Y. Quantum Interference Channeling at Graphene Edges. *Nano Lett.* **2010**, *10*, 943–947.
- (66) Tian, J.; Cao, H.; Wu, W.; Yu, Q.; Chen, Y. P. Direct Imaging of Graphene Edges: Atomic Structure and Electronic Scattering. *Nano Lett.* **2011**, *11*, 3663–3668.
- (67) Sakai, K.-i.; Takai, K.; Fukui, K.; Nakanishi, T.; Enoki, T. Honeycomb Superperiodic Pattern and Its Fine Structure Near the Armchair Edge of Graphene Observed by Low-Temperature Scanning Tunneling Microscopy. *Phys. Rev. B: Condens. Matter Mater. Phys.* **2010**, *81*, 235417.
- (68) Broers, A. N. Resolution Limits for Electron-Beam Lithography. *IBM J. Res. Dev.* **1988**, 32, 502–513.
- (69) Mistry, K. S.; Larsen, B. A.; Blackburn, J. L. High-Yield Dispersions of Large-Diameter Semiconducting Single-Walled Carbon Nanotubes with Tunable Narrow Chirality Distributions. *ACS Nano* **2013**, *7*, 2231–2239.
- (70) Way, A. J.; Murray, E. A.; Göltl, F.; Saraswat, V.; Jacobberger, R. M.; Mavrikakis, M.; Arnold, M. S. Anisotropic Synthesis of Armchair Graphene Nanoribbon Arrays from Sub-5 nm Seeds at

- Variable Pitches on Germanium. J. Phys. Chem. Lett. 2019, 10, 4266–4272.
- (71) Ghosh, A.; Clavel, M. B.; Nguyen, P. D.; Meeker, M. A.; Khodaparast, G. A.; Bodnar, R. J.; Hudait, M. K. Growth, Structural, and Electrical Properties of Germanium-on-Silicon Heterostructure by Molecular Beam Epitaxy. *AIP Adv.* **2017**, *7*, 095214.
- (72) Garbrecht, M.; Saha, B.; Schroeder, J. L.; Hultman, L.; Sands, T. D. Dislocation-Pipe Diffusion in Nitride Superlattices Observed in Direct Atomic Resolution. *Sci. Rep.* **2017**, *7*, 46092.
- (73) Abedin, A.; Asadollahi, A.; Garidis, K.; Hellstrom, P.-E.; Ostling, M. Epitaxial Growth of Ge Strain Relaxed Buffer on Si With Low Threading Dislocation Density. *ECS Trans.* **2016**, *75*, 615–621.
- (74) Ye, H.; Yu, J. Germanium Epitaxy on Silicon. Sci. Technol. Adv. Mater. 2014, 15, 024601.
- (75) Rastelli, A.; von Känel, H. Island Formation and Faceting in the SiGe/Si(001) System. Surf. Sci. 2003, 532–535, 769–773.
- (76) Higashitarumizu, N.; Ishikawa, Y. Enhanced Direct-Gap Light Emission from Si-Capped N<sup>+</sup>-Ge Epitaxial Layers on Si After Post-Growth Rapid Cyclic Annealing: Impact of Non-Radiative Interface Recombination Toward Ge/Si Double Heterostructure Lasers. *Opt. Express* **2017**, 25, 21286–21300.
- (77) Gavelle, M.; Bazizi, E. M.; Scheid, E.; Fazzini, P. F.; Cristiano, F.; Armand, C.; Lerch, W.; Paul, S.; Campidelli, Y.; Halimaoui, A. Detailed Investigation of Ge-Si Interdiffusion in the Full Range of  $\operatorname{Si}_{1-x}\operatorname{Ge}_x (0 \leq x \leq 1)$  Composition. *J. Appl. Phys.* **2008**, *104*, 113524.
- (78) Kim, H. J.; Park, Y.; Bae, H. B.; Choi, S. H. High-Electron-Mobility SiGe on Sapphire Substrate for Fast Chipsets. *Adv. Condens. Matter Phys.* **2015**, 2015, 785415.
- (79) Scholz, R.; Gösele, U.; Niemann, E.; Wischmeyer, F. Micropipes and Voids at  $\beta$ -SiC/Si(100) Interfaces: An Electron Microscopy Study. *Appl. Phys. A: Mater. Sci. Process.* **1997**, *64*, 115–125.
- (80) Ferrari, A. C.; Basko, D. M. Raman Spectroscopy as a Versatile Tool for Studying the Properties of Graphene. *Nat. Nanotechnol.* **2013**, *8*, 235–246.
- (81) Luan, H.-C.; Lim, D. R.; Lee, K. K.; Chen, K. M.; Sandland, J. G.; Wada, K.; Kimerling, L. C. High-Quality Ge Epilayers on Si With Low Threading-Dislocation Densities. *Appl. Phys. Lett.* **1999**, 75, 2909–2911
- (82) Matthews, J. W. Defects Associated With the Accommodation of Misfit Between Crystals. J. Vac. Sci. Technol. 1975, 12, 126–133.
- (83) Maras, E.; Pizzagalli, L.; Ala-Nissila, T.; Jonsson, H. Atomic Scale Formation Mechanism of Edge Dislocation Relieving Lattice Strain in a GeSi Overlayer on Si(001). Sci. Rep. 2017, 7, 11966.